Journal of

Applied and Computational Mechanics

Shahid Chamran
University of Ahvaz

Research Paper

Power Law Nanofluid through Tapered Artery based on a Consistent Couple Stress Theory

Fatemeh Karami[1], Afshin Ahmadi Nadooshan[2], Yaghoub Tadi Beni[3]

[1] Department of Mechanical Engineering, Lorestan University, Khoramabad, Iran, Email: karamif.mech@gmail.com

[2] Department of Mechanical Engineering, Shahrekord University, Shahrekord, Iran, Email: ahmadi@sku.ac.ir

[3] Department of Mechanical Engineering, Shahrekord University, Shahrekord, Iran, Email: tadi@sku.ac.ir

Abstract. Based on couple stress theory, this study investigated non-Newtonian power-law nanofluid flows in converging, non-tapered, and diverging arteries. In addition to excluding gravity effects artery, geometry included mild stenosis. The momentum equation is solved via the Galerkin method, and the results are compared with experimental and classical findings. Although the power-law couple stress theory's relations are first used in the analysis of non-Newtonian blood flow, the results of this theory are far more consistent with experimental results than classical results. Comparison of the results of the study of blood flow velocity profiles in a non-tapered artery without stenosis by the mentioned theory with experimental and classical theory results shows the difference in velocity at the center of the artery between the experimental results and the results of the classical theory is 36%, while this value has been reduced to 14% for the results of the couple stress theory. The variations in velocity profile with the power-law index (n=0.8 and n=0.85) and the dimensionless Darcy number (Da=10^{-10} and Da=10^{-7}) in all three geometries indicated a flat velocity distribution with the increase in the power-law index while increasing the velocity profile with increased Darcy number. Mass transfer and energy equations are solved using the extended Kantorovich method. The solution convergence is evaluated, and the influence of parameters such as Prandtl number, Schmidt number, and dimensionless thermospheric and Brownian parameters on concentration and temperature profiles is obtained.

Keywords: Couple stress theory, nanoparticle, power-law model, tapered artery, blood flow.

1. Introduction

Many researchers are interested in investigating arterial blood flow and its main attributes such as velocity, pressure, and shear stress. Such attributes are applicable in diagnosing and treating disorders such as atherosclerosis. Atherosclerosis is a disease in which the arterial diameter is reduced and obstructed due to lipid accumulation on arterial walls [1]. As a result, there have been numerous studies on the effect of stenosis geometry on blood flow. Haldar [2] studied blood flow in an artery with mild stenosis to investigate the effect of stenosis geometry. In his study, the flow resistance decreased with a change in stenosis geometry, with the most resistance produced by symmetrical stenosis.

Nevertheless, stenosis is not the only geometric parameter influencing blood flow. Some studies have aimed to analyze the effect of the convergence/divergence of the arterial wall. Nadeem et al. [3] studied the power-law blood flow in a tapered stenosis artery, finding the effect of tapered geometry and stenosis on parameters such as impedance, shear stress, and flow velocity. Their results indicate a higher velocity in diverging tapered forms compared to direct and converging arteries at the same interval. Liu et al. [4] used a limited element method to solve pulsatile blood flow in tapered stenosis arteries numerically and obtained wall shear stress distribution. Their study correctly shows flow disturbance at the stenosis region, especially the neck and downstream parts leading to separation after the stenosis region.

In their study on non-Newtonian arterial blood flow, Shukla et al. [5] showed that while flow resistance and wall shear stress increase with increased stenosis, such increases are negligible due to the non-Newtonian behavior of blood. This clearly shows the significance of blood rheology on flow parameters. Johnston et al. [6] conducted a study on non-Newtonian blood flow in the right coronaries of humans, finding that the Newtonian blood viscosity model only performs well in regions with moderate to high shear stress, while the extended power-law model gives better results in regions with low shear stress. Liu and Tang [7] investigated the effects of the non-Newtonian attributes of blood on the shear stress of the coronary wall using numerical modeling of Newtonian and non-Newtonian models. Their study indicates that blood viscosity significantly influences wall shear stress, especially at the disturbance points. In a similar numerical study by Chen and Lu [8] on non-Newtonian fluid flow in a two-branch arterial model with a non-flat branch, the difference in results between Newtonian and non-Newtonian fluids was

significant, indicating the non-Newtonian attributes as an essential hemodynamic factor affecting the biology, pathology, and formation of atherosclerosis.

Most studies are based on Navier–Stokes classical theory; however, due to the length parameter and couple stresses in small-scale (nano and micro scales), flow studies are increasingly investigating newer theories such as the couple stress theory [9, 10]. Valanis and Sun [11] studied the Poiseuille flow of blood as a couple stress fluid and compared the velocity profiles obtained from the theory with experimental results, finding that blood flow can be described via the linear couple stress theory. Srivastava [12] investigated the effects of mild, symmetrical axial stenosis on blood flow based on couple stress fluid flow. The study shows increased flow resistance and wall shear stress at specific stenosis with reduced couple stress, while the flow resistance and wall couple stress in the couple stress fluid model were more significant compared to the Newtonian fluid model based on Navier–Stokes equations. In another numerical study by Srinivasacharya and Rao [13] on pulsatile blood flow in a two-branch artery with mild stenosis in the main artery based on Stokes's couple stress theory [14], flow parameters such as impedance, flow rate, and shear stress were influenced by the parameters of couple stress fluid. According to their results, impedance, flow rate, and shear stress increased with an increase in couple stress fluid parameters.

In the present study, blood is considered a nanofluid. Nanofluid combines nano-sized metal or non-metallic particles and a base fluid with various applications in the energy, medical, electronics, and food industries [15-17]. Pordanjani et al. [15] examine the applications and effects of nanofluids in energy systems. According to this study, nanofluids have improved heat transfer in a system in most studies. A similar result has been observed in improving microstructure energy efficiency [16]. Sheikhpour et al. [18] have studied the application of nanofluids in biomedicine, especially in drug delivery, imaging, and antibacterial activities. One of the applications of nanofluid drugs is to prevent the accumulation of blood cells. The inner walls of blood vessels are negatively charged. Therefore, to prevent the accumulation of blood cells, therapeutic particles must have a negative charge to prevent the accumulation.

In addition, the study of non-Newtonian fluid flow within the geometry of straight and conical tubes has many applications in industry. For example, in some studies, the flow of gels, considered non-Newtonian fluids, has been studied in converging tubes and tapered injectors. Gel propellants are composed of liquid fuels and gelling agents that improve the rheological properties of the fuel and thus the combustion efficiency [19].

Whereas other studies based on couple stress theory on blood flow are based on Newtonian fluid, this paper investigates a power-law fluid flow in tapered and non-tapered arteries with mild stenosis using the couple stress theoretical and extended relations proposed by Karami et al. [20]. It models blood as a nanofluid, considering its suspension property. Energy and mass transfer equations are solved with momentum equations. Many studies have been on blood flow in tapered arteries where many terms of the energy and mass transfer equations are omitted using dimensional analysis and gravitational effects [21-23], or only momentum equation is used [24-26]. Nevertheless, this study avoids much of the mentioned simplifications and proposes a more comprehensive solution for mass transfer and energy equations based on an utterly consistent couple stress theory.

2. Geometry, Equations, and Boundary Conditions

The laminar flow of an incompressible, non-Newtonian power-law nanofluid is assumed in the 2D geometry of a tapered artery (Fig. 1). The stenosis is assumed to be mild, and wall geometry for the converging and diverging tapered and non-tapered arteries at the stenosis point is as follows [27]:

$$R(z) = d(z)\left[1 - \Psi\left(l_0^{m-1}(z - d_0) - (z - d_0)^m\right)\right], \quad d_0 < z \le d_0 + l_0 \tag{1}$$

At the non-stenosis region, the flow is modeled by:

$$R(z) = d(z) \tag{2}$$

In the above equations:

$$\Psi = \frac{\delta m^{\frac{m}{m-1}}}{R_0 l_0^m (m-1)} \tag{3}$$

$$d(z) = R_0 + \xi z \tag{4}$$

where $R(z)$, l_0, d_0 and R_0 are the radius of the tapered stenosis region, length of the stenosis region, distance from the inlet to the stenosis, and radius of the non-stenosis tube and δ is Maximum stenosis height occurring at $z = d_0 + l_0 m^{-1/(m-1)}$. m is the parameter denoting stenosis shape and determining the stenosis curve. $m = 2$ means a symmetric stenosis. Regardless of the gravitational force effects, the equations and boundary conditions governing flow are [23]:

$$\nabla \cdot V = 0 \tag{5}$$

$$\rho_{nf}\frac{DV}{Dt} = -\nabla P + \nabla \cdot A \tag{6}$$

$$\frac{DC}{Dt} = D_B \nabla^2 C + \left(\frac{D_T}{T_0}\right)\nabla^2 T \tag{7}$$

$$(\rho c)_{nf}\frac{DT}{Dt} = K_{nf}\nabla^2 T + (\rho c)_p\left[D_B \nabla C.\nabla T + \left(\frac{D_T}{T_0}\right)\nabla T.\nabla T\right] \tag{8}$$

$$\frac{\partial u}{\partial r} = 0, \frac{\partial T}{\partial r} = 0, \frac{\partial C}{\partial r} = 0 \qquad \text{at } r = 0, \tag{9}$$

$$u = u_B, M_z = 0, T = T_1, C = C_1 \quad \text{at } r = R(z), \tag{10}$$

$$\frac{\partial u}{\partial r} = \frac{\alpha}{\sqrt{\lambda}} \left(u_B - u_f \right), u_f = -\frac{\lambda}{\mu} \frac{dP}{dz} \quad \text{at } r = R(z), \tag{11}$$

$$\frac{\partial T}{\partial z} = 0, \frac{\partial C}{\partial z} = 0 \quad \text{at } z = l_1. \tag{12}$$

where V is the velocity vector, ρ_{nf} is density, P is the pressure, f is the body force, C is the nanoparticle concentration, D_B and D_T are the Brownian and Thermospheric diffusion coefficients, respectively, T is the temperature, K_{nf} is the thermal conductivity coefficient, u_f and u_B are the filtration velocity and the slip velocity on the wall, respectively. λ is the wall permeability coefficient, T_1 and C_1 are the nanofluid temperature and nanofluid concentration on the wall, respectively. α is a dimensionless quantity dependent on material parameters. It indicates a porous material structure at the boundary region and l_1 is the length of the artery. Eqs. (9) and (10) respectively show the wall's axial symmetry, slip velocity, and zero moment. Eq. (11) indicates arterial wall permeability [28], while Eq. (12) represents the temperature and concentration development at the arterial end. A is a stress tensor consisting of two symmetric and asymmetric components. The symmetric component of the stress tensor is obtained by [20]:

$$A_{(ji)} = -P\delta_{ij} + 2\mu_{eff} D_{ij} \tag{13}$$

$$D_{ij} = v_{(i,j)} = \frac{1}{2} \left(v_{i,j} + v_{j,i} \right) \tag{14}$$

$$\mu_{eff} = k \left(v_{i,j} + v_{j,i} \right)^{n-1} \tag{15}$$

$$M_{ji} = \varepsilon_{ijk} M_k \tag{16}$$

where D_{ij}, μ_{eff}, k, M_{ji} and M_k are the symmetric component of velocity gradient tensor, the effective viscosity of the power-law fluid, the flow consistency index, the character of the couple stress tensor, and the character of couple stress vector, respectively. The asymmetric component of stress tensor for a power-law, non-Newtonian fluid is given by [20]:

$$A_{[ji]} = M_{[i,j]} = -\frac{1}{2} \left[M_{i,j} - M_{j,i} \right] = -l^2 k \begin{bmatrix} (n-1)\left(-\left(v_{i,j} + v_{j,i} \right) \right)^{n-2} \left(-\left(v_{i,jj} + v_{j,ij} \right) \right) \left(v_{k,ki} - v_{i,kk} \right) + \left(-\left(v_{i,j} + v_{j,i} \right) \right)^{n-1} \left(v_{k,kij} - v_{i,kkj} \right) \\ -(n-1)\left(-\left(v_{i,j} + v_{j,i} \right) \right)^{n-2} \left(-\left(v_{j,ii} + v_{i,ji} \right) \right) \left(v_{k,kj} - v_{j,kk} \right) - \left(-\left(v_{i,j} + v_{j,i} \right) \right)^{n-1} \left(v_{k,kji} - v_{j,kki} \right) \end{bmatrix} \tag{17}$$

where $M_{i,j}$ is the gradient vector of couple stress and l is the characteristic length missing in classical relations. The mentioned characteristic length depends on the geometry, boundary conditions, and default conditions of the problems and maybe obtained via tests or molecular simulation. Section 3-3 elaborates on this parameter. In Eq. (17), the shear rate, shear stress, and couple stress have negative signs because the studied geometry resembles a tube.

Ultimately, tension tensor consisting of both symmetric and asymmetric components is given by:

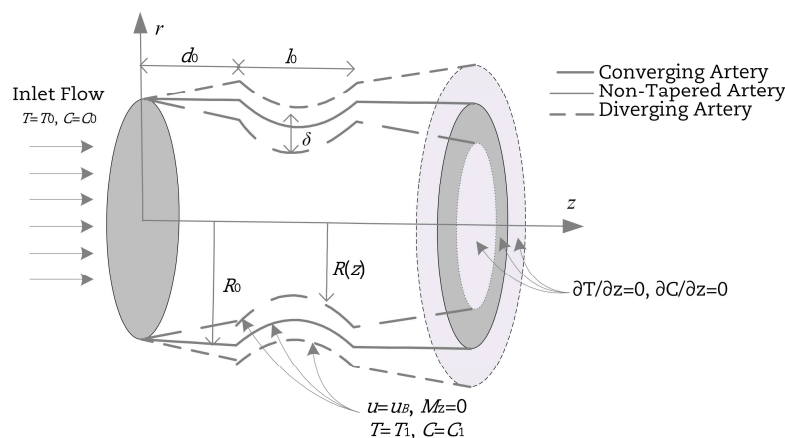$$A_{ji} = A_{(ji)} + A_{[ji]} \tag{18}$$

Fig. 1. The geometry of non-tapered and tapered arteries [27]

Fluid flow equations (Eqs. (5-8)) in cylindrical coordinates are non-dimensionalized by these dimensionless parameters:

$$L^* = \frac{l}{R_0} \ , \ \ \Pr = \frac{\nu}{\alpha_1} \ , \ \ \overline{P} = \frac{R_0 P}{U \mu_{nd}} \ , \ \ \overline{u} = \frac{u}{U} \ , \ \ \overline{v} = \frac{l_0}{\delta U} v \ , \ \ \overline{r} = \frac{r}{R_0} \ , \ \ \mathrm{Re} = \frac{R_0 U}{\nu} \ , \ \ \mathrm{Sc} = \frac{\nu}{D_B} \ , \ \ \mu_{nd} = \frac{k U^{n-1}}{R_0^{n-1}} \ , \ \ \theta = \frac{T - T_1}{T_0 - T_1} \ ,$$

$$\sigma = \frac{C - C_1}{C_0 - C_1} \ , \ \ \overline{z} = \frac{z}{R_0} \ , \ \ N_b = \frac{(\rho c)_p D_B (C_0 - C_1)}{(\rho c)_{nf} \alpha_1} \ , \ \ N_t = \frac{(\rho c)_p D_T (T_0 - T_1)}{(\rho c)_{nf} \alpha_1 T_0} \ , \ \ \alpha_1 = \frac{K_{nf}}{\rho_{nf} c_p}$$

(19)

where U is the mean velocity at each flow cross-section. Initially, the continuity equation is non-dimensionalized:

$$\left(\frac{\delta}{R_0} \right) \frac{1}{\overline{r}} \frac{\partial}{\partial \overline{r}} (\overline{r} \overline{v}) + \frac{\partial}{\partial \overline{z}} \overline{u} = 0$$

(20)

Dimensional analysis of Eq. (20), assuming mild arterial wall stenosis ($O(\delta / R_0) << 1$) and the satisfaction of ($O(R_0 / l_0) = 1$) is given by:

$$\left(\frac{\delta}{R_0} \right) \frac{1}{\overline{r}} \frac{\partial}{\partial \overline{r}} (\overline{r} \overline{v}) + \frac{\partial \overline{u}}{\partial \overline{z}} = 0$$

$$O\left(\frac{\delta}{R_0} \right) \qquad O(1)$$

(21)

Therefore, Eq. (21) leads to $O(\partial \overline{u} / \partial \overline{z}) = O(\delta / R_0)$.

To non-dimensionalize and simplify momentum equations in z and r directions, stress is first calculated:

$$A_{(rr)} = -P + k \left(2 \frac{\partial v}{\partial r} \right)^n$$

(22)

$$A_{[rr]} = 0$$

(23)

$$A_{(zr)} = k \left(\frac{\partial v}{\partial z} + \frac{\partial u}{\partial r} \right)^n$$

(24)

$$A_{[zr]} = -l^2 k \left[-(n-1) \left(-\left(\frac{\partial v}{\partial z} + \frac{\partial u}{\partial r} \right) \right)^{n-2} \left(-\left(\frac{\partial^2 v}{\partial z^2} + \frac{\partial}{\partial z} \left(\frac{\partial u}{\partial r} \right) \right) \right) \left(\frac{\partial^2 v}{\partial z^2} \right) \left(\frac{2}{r} \frac{\partial}{\partial r} \left(r \frac{\partial v}{\partial r} \right) \right) - \frac{1}{r} \frac{\partial}{\partial r} \left(r \frac{\partial v}{\partial r} \right) - \frac{\partial^2 v}{\partial z^2} \right) - (n-1) \left(-2 \frac{\partial v}{\partial r} \right)^{n-2} \left(\frac{2}{r} \frac{\partial}{\partial r} \left(r \frac{\partial v}{\partial r} \right) \right) \left(\frac{\partial^2 v}{\partial z^2} + \frac{1}{r} \frac{\partial}{\partial r} \left(r \frac{\partial v}{\partial r} \right) \right) \right]$$

(25)

$$A_{(zz)} = -P + k \left(2 \frac{\partial u}{\partial z} \right)^n$$

(26)

$$A_{[zz]} = 0$$

(27)

$$A_{[rz]} = -l^2 k \left[\begin{array}{l} -(n-1) \left(-\left(\frac{\partial u}{\partial r} + \frac{\partial v}{\partial z} \right) \right)^{n-2} \left(-\left(\left(\frac{\partial^2 u}{\partial r^2} \right) + \frac{\partial}{\partial r} \left(\frac{\partial v}{\partial z} \right) \right) \right) \left(\frac{\partial^2 u}{\partial z^2} + \frac{1}{r} \frac{\partial}{\partial r} \left(r \frac{\partial u}{\partial r} \right) \right) - \left(-\left(\frac{\partial u}{\partial r} + \frac{\partial v}{\partial r} \right) \right)^{n-1} \frac{\partial}{\partial r} \left(\frac{\partial^2 u}{\partial z^2} + \frac{1}{r} \frac{\partial}{\partial r} \left(r \frac{\partial u}{\partial r} \right) \right) \\ + (n-1) \left(-\left(\frac{\partial u}{\partial r} + \frac{\partial v}{\partial z} \right) \right)^{n-2} \left(-\left(\frac{\partial^2 v}{\partial z^2} + \frac{\partial^2 u}{\partial z \partial r} \right) \right) \left(\frac{\partial^2 v}{\partial z^2} + \frac{1}{r} \frac{\partial}{\partial r} \left(r \frac{\partial v}{\partial r} \right) \right) + \left(-\left(\frac{\partial u}{\partial r} + \frac{\partial v}{\partial z} \right) \right)^{n-1} \frac{\partial}{\partial z} \left(\frac{\partial^2 v}{\partial z^2} + \frac{1}{r} \frac{\partial}{\partial r} \left(r \frac{\partial v}{\partial r} \right) \right) \end{array} \right]$$

(28)

Moreover, shear stress has a negative sign:

$$S_{zr} = -\left(A_{(zr)} + A_{[zr]} \right)$$

(29)

$$S_{rz} = -\left(A_{(rz)} + A_{[rz]} \right)$$

(30)

where S_{zr} and S_{rz} are the shear stress tensor parameters. Substituting stress in the momentum Equation, extending it in the r direction and non-dimensionalization, and dimensional analysis (assuming $O(R_0 / L_0) = 1$ and $O(\delta / R_0) << 1$), we have:

$$\frac{\partial \overline{P}}{\partial \overline{r}} = 0$$

(31)

Further, Eq. (31) gives:

$$\overline{P} = \overline{P}(\overline{z})$$

(32)

Substituting the symmetric and asymmetric stress tensors in Eq. (18) yields the total stress tensor. Then we substitute it in:

$$\rho_{nf} \left(u \frac{\partial u}{\partial z} + v \frac{\partial u}{\partial r} \right) = \frac{1}{r} \frac{\partial}{\partial r} \left(r \left(S_{(rz)} + S_{[rz]} \right) \right) + \frac{\partial}{\partial z} \left(A_{(zz)} + A_{[zz]} \right)$$

(33)

By non-dimensionalizing and dimensional analysis of the above equation, the momentum equation in the z-direction is simplified:

$$-\frac{\partial \overline{P}}{\partial \overline{z}} - \frac{1}{\overline{r}}\frac{\partial}{\partial \overline{r}}\left(\overline{r}\left(-\frac{\partial \overline{u}}{\partial \overline{r}}\right)^n\right) + L^{*2}\frac{1}{\overline{r}}\frac{\partial}{\partial \overline{r}}\left(\overline{r}\left((n-1)\left(-\frac{\partial \overline{u}}{\partial \overline{r}}\right)^{n-2}\left(\frac{\partial^2 \overline{u}}{\partial \overline{r}^2}\right)\left(\frac{1}{\overline{r}}\frac{\partial}{\partial \overline{r}}\left(\overline{r}\frac{\partial \overline{u}}{\partial \overline{r}}\right)\right)\right)\right) + L^{*2}\frac{1}{\overline{r}}\frac{\partial}{\partial \overline{r}}\left(\overline{r}\left(-\frac{\partial \overline{u}}{\partial \overline{r}}\right)^{n-1}\frac{\partial}{\partial \overline{r}}\left(-\frac{1}{\overline{r}}\frac{\partial}{\partial \overline{r}}\left(\overline{r}\frac{\partial \overline{u}}{\partial \overline{r}}\right)\right)\right) = 0 \qquad (34)$$

Mass transfer and energy equations are non-dimensionalized via Eqs. (21) and (19) and then simplified using dimensional analysis:

$$\mathrm{Sc}\,\mathrm{Re}\,\overline{u}\frac{\partial \sigma}{\partial \overline{z}} = \left[\frac{1}{\overline{r}}\frac{\partial}{\partial \overline{r}}(\overline{r}\frac{\partial \sigma}{\partial \overline{r}}) + \frac{\partial^2 \sigma}{\partial \overline{z}^2}\right] + \frac{N_t}{N_b}\left[\frac{1}{\overline{r}}\frac{\partial}{\partial \overline{r}}(\overline{r}\frac{\partial \theta}{\partial \overline{r}}) + \frac{\partial^2 \theta}{\partial \overline{z}^2}\right] \qquad (35)$$

$$\mathrm{Pr}\,\mathrm{Re}\,\overline{u}\frac{\partial \theta}{\partial \overline{z}} = \frac{1}{\overline{r}}\frac{\partial}{\partial \overline{r}}(\overline{r}\frac{\partial \theta}{\partial \overline{r}}) + \frac{\partial^2 \theta}{\partial \overline{z}^2} + N_b\left[\frac{\partial \sigma}{\partial \overline{r}}\frac{\partial \theta}{\partial \overline{r}} + \frac{\partial \sigma}{\partial \overline{z}}\frac{\partial \theta}{\partial \overline{z}}\right] + N_t\left[\left(\frac{\partial \theta}{\partial \overline{r}}\right)^2 + \left(\frac{\partial \theta}{\partial \overline{z}}\right)^2\right] \qquad (36)$$

The dimensionless boundary conditions according to Eqs. (9-12) are:

$$\frac{\partial \overline{u}}{\partial \overline{r}}(0) = 0, \frac{\partial \sigma}{\partial \overline{r}}(0,\overline{z}) = 0, \frac{\partial \theta}{\partial \overline{r}}(0,\overline{z}) = 0, \qquad (37)$$

$$\overline{u}\left(R^*\right) = U_B, \sigma\left(R^*,\overline{z}\right) = 0, \theta\left(R^*,\overline{z}\right) = 0 \qquad (38)$$

$$\frac{1}{\overline{r}}\frac{\partial}{\partial \overline{r}}\left(\overline{r}\frac{\partial \overline{u}}{\partial \overline{r}}\right) = 0, \frac{\partial \overline{u}}{\partial \overline{r}} = \frac{R_0 \alpha}{\sqrt{\lambda}}\left(U_B - U_f\right), U_f = -D_a\frac{d\overline{P}}{d\overline{z}}, D_a = \frac{\lambda}{R_0^{~2}}\ \text{ at }\ \overline{r} = R^*, \qquad (39)$$

$$\sigma\left(\overline{r},0\right) = 1, \frac{\partial \sigma}{\partial \overline{z}}\left(\overline{r},L\right) = 0, \theta\left(\overline{r},0\right) = 1, \frac{\partial \theta}{\partial \overline{z}}\left(\overline{r},L\right) = 0. \qquad (40)$$

where L is the dimensionless length of the artery in Eq. (40).

3. Solution of the Equations

3.1 Solution of the Momentum Equation by Galerkin Method

The momentum equation (Eq. (34)) is solved using the Galerkin method. Accordingly, first, the desired solution for velocity profile is selected [29]:

$$\overline{u} = U_B + \sum_{j=1}^{3} c_j \varphi_j\left(x\right) \qquad (41)$$

φ_1, φ_2 and φ_3 are the basic functions of the boundary condition, obtained from solving three third-degree equations according to the boundary conditions of Eqs. (37-39):

$$\varphi_1\left(\overline{r}\right) = \frac{1}{6}\overline{r}^3 - \frac{3}{8}R^*\overline{r}^2 + \frac{5}{24}R^{*3} \qquad (42)$$

$$\varphi_2\left(\overline{r}\right) = \frac{1}{24}\overline{r}^4 - \frac{1}{6}R^{*2}\overline{r}^2 + \frac{1}{8}R^{*4} \qquad (43)$$

$$\varphi_3\left(\overline{r}\right) = \frac{1}{60}\overline{r}^5 - \frac{5}{48}R^{*3}\overline{r}^2 + \frac{7}{80}R^{*5} \qquad (44)$$

As a result, using the Galerkin method, the functions φ_1, φ_2 and φ_3 are chosen as weighting functions. Multiplying each of them by Eq. (34) and integrating within the solution domain gives a system of equations which can yield the constant values c_1, c_2 and c_3:

$$\int_0^{R^*} \varphi_1\left(\overline{r}\right)\left\{\begin{array}{l} -\dfrac{\partial \overline{P}}{\partial \overline{z}} - \dfrac{1}{\overline{r}}\dfrac{\partial}{\partial \overline{r}}\left(\overline{r}\left(-\dfrac{\partial}{\partial \overline{r}}\left(U_B + \sum_{j=1}^{3}c_j\varphi_j\left(x\right)\right)\right)^n\right) + L^{*2}\dfrac{1}{\overline{r}}\dfrac{\partial}{\partial \overline{r}}\left(\overline{r}\left((n-1)\left(-\dfrac{\partial}{\partial \overline{r}}\left(U_B + \sum_{j=1}^{3}c_j\varphi_j\left(x\right)\right)\right)^{n-2}\left(\dfrac{\partial^2 \overline{u}}{\partial \overline{r}^2}\right)\left(\dfrac{1}{\overline{r}}\dfrac{\partial}{\partial \overline{r}}\left(\overline{r}\dfrac{\partial}{\partial \overline{r}}\left(U_B + \sum_{j=1}^{3}c_j\varphi_j\left(x\right)\right)\right)\right)\right)\right) \\ + L^{*2}\dfrac{1}{\overline{r}}\dfrac{\partial}{\partial \overline{r}}\left(\overline{r}\left(-\dfrac{\partial}{\partial \overline{r}}\left(U_B + \sum_{j=1}^{3}c_j\varphi_j\left(x\right)\right)\right)^{n-1}\dfrac{\partial}{\partial \overline{r}}\left(-\dfrac{1}{\overline{r}}\dfrac{\partial}{\partial \overline{r}}\left(\overline{r}\dfrac{\partial}{\partial \overline{r}}\left(U_B + \sum_{j=1}^{3}c_j\varphi_j\left(x\right)\right)\right)\right)\right) \end{array}\right\} d\overline{r} = 0 \qquad (45)$$

$$\int_0^{R^*} \varphi_2(\overline{r}) \left\{ \begin{array}{l} \left[-\dfrac{\partial \overline{P}}{\partial \overline{z}} - \dfrac{1}{\overline{r}}\dfrac{\partial}{\partial \overline{r}}\left(\overline{r}\left(-\dfrac{\partial}{\partial \overline{r}}\left(U_B + \sum\limits_{j=1}^{3} c_j \varphi_j(x) \right) \right)^n \right) + L^{*2}\dfrac{1}{\overline{r}}\dfrac{\partial}{\partial \overline{r}}\left(\overline{r}\left((n-1)\left(-\dfrac{\partial}{\partial \overline{r}}\left(U_B + \sum\limits_{j=1}^{3} c_j \varphi_j(x) \right) \right)^{n-2} \left(\dfrac{\partial^2 \overline{u}}{\partial \overline{r}^2} \right)\left(\dfrac{1}{\overline{r}}\dfrac{\partial}{\partial \overline{r}}\left(\overline{r}\dfrac{\partial}{\partial \overline{r}}\left(U_B + \sum\limits_{j=1}^{3} c_j \varphi_j(x) \right) \right) \right) \right) \right] \\ + L^{*2}\dfrac{1}{\overline{r}}\dfrac{\partial}{\partial \overline{r}}\left(\overline{r}\left(-\dfrac{\partial}{\partial \overline{r}}\left(U_B + \sum\limits_{j=1}^{3} c_j \varphi_j(x) \right) \right)^{n-1}\dfrac{\partial}{\partial \overline{r}}\left(-\dfrac{1}{\overline{r}}\dfrac{\partial}{\partial \overline{r}}\left(\overline{r}\dfrac{\partial}{\partial \overline{r}}\left(U_B + \sum\limits_{j=1}^{3} c_j \varphi_j(x) \right) \right) \right) \right) \end{array} \right\} d\overline{r} = 0 \tag{46}$$

$$\int_0^{R^*} \varphi_3(\overline{r}) \left\{ \begin{array}{l} \left[-\dfrac{\partial \overline{P}}{\partial \overline{z}} - \dfrac{1}{\overline{r}}\dfrac{\partial}{\partial \overline{r}}\left(\overline{r}\left(-\dfrac{\partial}{\partial \overline{r}}\left(U_B + \sum\limits_{j=1}^{3} c_j \varphi_j(x) \right) \right)^n \right) + L^{*2}\dfrac{1}{\overline{r}}\dfrac{\partial}{\partial \overline{r}}\left(\overline{r}\left((n-1)\left(-\dfrac{\partial}{\partial \overline{r}}\left(U_B + \sum\limits_{j=1}^{3} c_j \varphi_j(x) \right) \right)^{n-2} \left(\dfrac{\partial^2 \overline{u}}{\partial \overline{r}^2} \right)\left(\dfrac{1}{\overline{r}}\dfrac{\partial}{\partial \overline{r}}\left(\overline{r}\dfrac{\partial}{\partial \overline{r}}\left(U_B + \sum\limits_{j=1}^{3} c_j \varphi_j(x) \right) \right) \right) \right) \right] \\ + L^{*2}\dfrac{1}{\overline{r}}\dfrac{\partial}{\partial \overline{r}}\left(\overline{r}\left(-\dfrac{\partial}{\partial \overline{r}}\left(U_B + \sum\limits_{j=1}^{3} c_j \varphi_j(x) \right) \right)^{n-1}\dfrac{\partial}{\partial \overline{r}}\left(-\dfrac{1}{\overline{r}}\dfrac{\partial}{\partial \overline{r}}\left(\overline{r}\dfrac{\partial}{\partial \overline{r}}\left(U_B + \sum\limits_{j=1}^{3} c_j \varphi_j(x) \right) \right) \right) \right) \end{array} \right\} d\overline{r} = 0 \tag{47}$$

Substituting the basic functions φ_j (Eqs. (42-44)) and constant values c_j in Eq. (41) gives the arterial flow velocity profile:

3.2 Solution of Mass Transfer and Energy Equations by EKM

The extended Kantorovich method (EKM) is used to solve coupled equations (Eqs. (35) and (36)). In EKM, there is a multiplication of two independent functions for each unknown. Commonly, one of the independent functions is approximated based on boundary conditions, and after placing the functions in respective equations, using the Galerkin method, the resulting equations are multiplied by the weighting functions. After integrating within the solution domain, a differential equation is obtained, solvable using numerical or analytical methods. This process is repeated until reaching convergence and the final answer [30].

Following the above, concentration and temperature functions are:

$$\sigma(\overline{r},\overline{z}) = \psi_{1n}(\overline{z})\xi_{1n}(\overline{r}) + S(\overline{r},\overline{z}) \tag{48}$$

$$\theta(\overline{r},\overline{z}) = \psi_{2n}(\overline{z})\xi_{2n}(\overline{r}) + S(\overline{r},\overline{z}) \tag{49}$$

where the n symbol indicates the degree of repetitions to obtain the convergency.

The $S(\overline{r},\overline{z})$ function is selected based on the boundary conditions of Eqs. (37), (38) and (40) and for the sake of homogeneity in boundary conditions:

$$S(\overline{r},\overline{z}) = \sum_{n=0}^{\infty} \frac{4(-1)^{\operatorname{csgn}\left(\frac{1}{R}\right)n} e^{\frac{\pi(1+2n)\operatorname{csgn}\left(\frac{1}{R}\right)z}{2R}} \cos\left(\frac{(1+2n)\pi \operatorname{csgn}\left(\frac{1}{R}\right)r}{2R} \right)\left(e^{\frac{(1+2n)\pi \operatorname{csgn}\left(\frac{1}{R}\right)(L-z)}{R}} + 1 \right)}{\left((1+2n)\pi + 2\cos\left(\frac{\operatorname{csgn}\left(\frac{1}{R}\right)\pi}{2} \right) \right)\left(e^{\frac{(1+2n)\pi \operatorname{csgn}\left(\frac{1}{R}\right)L}{R}} + 1 \right)} \tag{50}$$

Therefore, the boundary conditions of functions $\psi_i(\overline{z})$ and $\xi_i(\overline{r})$ are:

$$\psi_{in}(0) = 0, \psi_{in}{}'(L) = 0 \quad i = 1,2 \tag{51}$$

$$\xi_{in}(R^*) = 0, \xi_{in}{}'(0) = 0 \quad i = 1,2 \tag{52}$$

Substituting Eqs. (48) and (49) respectively in Eqs. (35) and (36) simplify mass transfer and energy equations:

$$\frac{1}{\overline{r}}\frac{\partial}{\partial \overline{r}}\left(\overline{r}\frac{\partial \xi_{1j}}{\partial \overline{r}} \right)\psi_{1j} + \left(1 + \frac{N_t}{N_b} \right)\left(\frac{1}{\overline{r}}\frac{\partial}{\partial \overline{r}}\left(\overline{r}\frac{\partial S}{\partial \overline{r}} \right) + \frac{\partial^2 S}{\partial \overline{z}^2} \right) + \xi_{1j}\frac{\partial^2 \psi_{1j}}{\partial \overline{z}^2} + \frac{N_t}{N_b}\psi_{2j}\frac{1}{\overline{r}}\frac{\partial}{\partial \overline{r}}\left(\overline{r}\frac{\partial \xi_{2j}}{\partial \overline{r}} \right) + \frac{N_t}{N_b}\xi_{2j}\frac{\partial^2 \psi_{2j}}{\partial \overline{z}^2} - Sc\,Re\,\overline{u}\xi_{1j}\frac{\partial \psi_{1j}}{\partial \overline{z}} - Sc\,Re\,\overline{u}\frac{\partial S}{\partial \overline{z}} = 0 \tag{53}$$

$$\frac{1}{\overline{r}}\frac{\partial}{\partial \overline{r}}\left(\overline{r}\frac{\partial \xi_{2j}}{\partial \overline{r}} \right)\psi_{2j} + \frac{1}{\overline{r}}\frac{\partial}{\partial \overline{r}}\left(\overline{r}\frac{\partial S}{\partial \overline{r}} \right) + \xi_{2j}\frac{\partial^2 \psi_{2j}}{\partial \overline{z}^2} + \frac{\partial^2 S}{\partial \overline{z}^2} + N_t\left\{ \left[\psi_{2j}\frac{\partial \xi_{2j}}{\partial \overline{r}} + \frac{\partial S}{\partial \overline{r}} \right]^2 + \left[\xi_{2n}\frac{\partial \psi_{2j}}{\partial \overline{z}} + \frac{\partial S}{\partial \overline{z}} \right]^2 \right\} - Pr\,Re\,\overline{u}\xi_{2j}\frac{\partial \psi_{2j}}{\partial \overline{z}} - Pr\,Re\,\overline{u}\frac{\partial S}{\partial \overline{z}}$$
$$+ N_b\left\{ \left[\psi_{1j}\frac{\partial \xi_{1j}}{\partial \overline{r}} + \frac{\partial S}{\partial \overline{r}} \right]\left[\psi_{2j}\frac{\partial \xi_{2j}}{\partial \overline{r}} + \frac{\partial S}{\partial \overline{r}} \right] + \left[\psi_{1j}\frac{\partial \xi_{1j}}{\partial \overline{r}} + \frac{\partial S}{\partial \overline{r}} \right]\left[\xi_{2j}\frac{\partial \psi_{2j}}{\partial \overline{z}} + \frac{\partial S}{\partial \overline{z}} \right] \right\} = 0 \tag{54}$$

The initial approximations for functions ξ_1 and ξ_2 according to the boundary conditions of Eqs. (37) and (38) are:

$$\xi_{10}(\overline{r}) = \frac{1}{4}\left(\overline{r}^2 - R^{*2} + \overline{r}^4 - R^{*4} \right) \tag{55}$$

$$\xi_{20}(\overline{r}) = -\left(\overline{r}^2 - R^{*2} + \overline{r}^6 - R^{*6} \right) \tag{56}$$

Substituting Eqs. (55) and (56) respectively in Eqs. (53) and (54), and then, respectively multiplying them by functions $\xi_{10}(\overline{r})$ and $\xi_{20}(\overline{r})$ followed by integrating into the solution domain [0-R*] gives:

$$F_{1j-1}\psi_{1j} + F_{2j-1} + F_{3j-1}\frac{d^2\psi_{1j}}{d\overline{z}^2} + F_{4j-1} + F_{5j-1}\psi_{2j} + F_{6j-1} + F_{7j-1}\frac{d^2\psi_{2j}}{d\overline{z}^2} + F_{8j-1} + F_{9j-1}\frac{\partial\psi_{1j}}{\partial\overline{z}} + F_{10j-1} = 0, j \geq 1 \tag{57}$$

$$G_{1j-1}\psi_{2j} + G_{2j-1} + G_{3j-1}\frac{d^2\psi_{2j}}{d\overline{z}^2} + G_{4j-1} + G_{5j-1}\psi_{1j}\psi_{2j} + G_{6j-1}\psi_{2j} + G_{7j-1}(\overline{z})\psi_{1j} + G_{8j-1} + G_{9j-1}\frac{d\psi_{1j}}{d\overline{z}}\frac{d\psi_{2j}}{d\overline{z}} + G_{10j-1}\frac{d\psi_{2j}}{d\overline{z}} + G_{11j-1}(\overline{z})\frac{d\psi_{1j}}{d\overline{z}} +$$
$$G_{12j-1} + G_{13j-1}\psi_{2j}{}^2 + G_{14j-1} + G_{15j-1}\psi_{2j} + G_{16j-1}\left(\frac{d\psi_{2j}}{d\overline{z}}\right)^2 + G_{17j-1} + G_{18j-1}\frac{d\psi_{2j}}{d\overline{z}} + G_{19j-1}\frac{d\psi_{2j}}{d\overline{z}} + G_{20j-1} = 0, j \geq 1 \tag{58}$$

The Galerkin method is used for each iteration to solve the above differential equations system; therefore, according to the boundary conditions of Eq. (51) and the descriptions on Galerkin method (Section 3.1), the functions $\psi_{1j}(\overline{z})$ and $\psi_{2j}(\overline{z})$ are defined as:

$$\psi_{1j}(\overline{z}) = \varepsilon_{1j}q_1(\overline{z}) + \varepsilon_{2j}q_2(\overline{z}) + \varepsilon_{3j}q_3(\overline{z}) \tag{59}$$

$$\psi_{2j}(\overline{z}) = \alpha_{1j}\left(\frac{1}{2}\overline{z}^2 - L\overline{z}\right) + \alpha_{2j}\left(\frac{1}{6}\overline{z}^3 - \frac{1}{2}L^2\overline{z}\right) + \alpha_{3j}\left(\frac{1}{12}\overline{z}^4 - \frac{1}{3}L^3\overline{z}\right) \tag{60}$$

$$q_1(\overline{z}) = \left(\frac{1}{2}\overline{z}^2 - L\overline{z}\right), q_2(\overline{z}) = \left(\frac{1}{6}\overline{z}^3 - \frac{1}{2}L^2\overline{z}\right), q_3(\overline{z}) = \left(\frac{1}{12}\overline{z}^4 - \frac{1}{3}L^3\overline{z}\right) \tag{61}$$

The constant values $\varepsilon_{ij}, i = 1,2,3$ and α_{ij} are obtained by substituting $\psi_{1j}(\overline{z})$ and $\psi_{2j}(\overline{z})$ in the system of equations below:

$$\int_0^L q_p(\overline{z})\left[F_{1j-1}\psi_{1j} + F_{2j-1} + F_{3j-1}\frac{d^2\psi_{1j}}{d\overline{z}^2} + F_{4j-1} + F_{5j-1}\psi_{2j} + F_{6j-1} + F_{7j-1}\frac{d^2\psi_{2j}}{d\overline{z}^2} + F_{8j-1} + F_{9j-1}\frac{\partial\psi_{1j}}{\partial\overline{z}} + F_{10j-1}\right]d\overline{z} = 0, p = 1,2,3. \tag{62}$$

$$\int_0^L q_p(\overline{z})\left[\begin{array}{l} G_{1j-1}\psi_{2j} + G_{2j-1} + G_{3j-1}\frac{d^2\psi_{2j}}{d\overline{z}^2} + G_{4j-1} + G_{5j-1}\psi_{1j}\psi_{2j} + G_{6j-1}\psi_{2j} + G_{7j-1}(\overline{z})\psi_{1j} + G_{8j-1} + G_{9j-1}\frac{d\psi_{1j}}{d\overline{z}}\frac{d\psi_{2j}}{d\overline{z}} + G_{10j-1}\frac{d\psi_{2j}}{d\overline{z}} \\ +G_{11j-1}(\overline{z})\frac{d\psi_{1j}}{d\overline{z}} + G_{12j-1} + G_{13j-1}\psi_{2j}{}^2 + G_{14j-1} + G_{15j-1}\psi_{2j} + G_{16j-1}\left(\frac{d\psi_{2j}}{d\overline{z}}\right)^2 + G_{17j-1} + G_{18j-1}\frac{d\psi_{2j}}{d\overline{z}} + G_{19j-1}\frac{d\psi_{2j}}{d\overline{z}} + G_{20j-1} \end{array}\right]d\overline{z} = 0, p = 1,2,3. \tag{63}$$

After that, using the values obtained for $\psi_{1j}(\overline{z})$ and $\psi_{2j}(\overline{z})$, and substituting them in Eqs. (53) and (54), and then, integrating within the dimensionless arterial length [0-L], we have two equations:

$$M_{1j}\frac{1}{\overline{r}}\frac{d}{d\overline{r}}\left(\overline{r}\frac{d\xi_{1j}}{d\overline{r}}\right) + M_{2j} + M_{3j}\xi_{1j} + M_{4j} + M_{5j}\frac{1}{\overline{r}}\frac{d}{d\overline{r}}\left(\overline{r}\frac{d\xi_{2j}}{d\overline{r}}\right) + M_{6j} + M_{7j}\xi_{2j} + M_{8j} + M_{9j}\xi_{1j} + M_{10j} = 0 \tag{64}$$

$$N_{1j}\frac{1}{\overline{r}}\frac{d}{d\overline{r}}\left(\overline{r}\frac{d\xi_{2j}}{d\overline{r}}\right) + N_{2j} + N_{3j}\xi_{2j} + N_{4j} + N_{5j}\frac{d\xi_{2j}}{d\overline{r}}\frac{d\xi_{2j}}{d\overline{r}} + N_{6j}\frac{d\xi_{2j}}{d\overline{r}} + N_{7j}\frac{d\xi_{1j}}{d\overline{r}} + N_{8j} + N_{9j}\xi_{1j}\xi_{2j} + N_{10j}\xi_{2j} + N_{11j}\xi_{1j}$$
$$+N_{12j} + N_{13j}\left(\frac{d\xi_{2j}}{d\overline{r}}\right)^2 + N_{14j} + N_{15j}\frac{d\xi_{2j}}{d\overline{r}} + N_{16j}\xi_{2j}{}^2 + N_{17j} + N_{18j}\xi_{2j} + N_{19j}\xi_{2j} + N_{20j} = 0 \tag{65}$$

Using Galerkin method and based on the boundary conditions in Eq. (52), ξ_{11} and ξ_{21} are given:

$$\xi_{1j}(\overline{r}) = \beta_{1j}x_1(\overline{r}) + \beta_{2j}x_2(\overline{r}) \tag{66}$$

$$\xi_{2j}(\overline{r}) = \beta_{3j}x_1(\overline{r}) + \beta_{4j}x_2(\overline{r}) \tag{67}$$

$$x_1(\overline{r}) = \overline{r}^2 - R^{*2}, x_1(\overline{r}) = \overline{r}^6 - R^{*6} \tag{68}$$

According to the boundary conditions, the functions in Eq. (68) are determined as desired. The constant values $\beta_{ij}, i = 1,2,3,4$ are obtained via the Galerkin method and by substituting Eqs. (66) and (67) in this system of equations:

$$\int_0^R x_p(\overline{r})\left[M_{1j}\frac{1}{\overline{r}}\frac{d}{d\overline{r}}\left(\overline{r}\frac{d\xi_{1j}}{d\overline{r}}\right) + M_{2j} + M_{3j}\xi_{1j} + M_{4j} + M_{5j}\frac{1}{\overline{r}}\frac{d}{d\overline{r}}\left(\overline{r}\frac{d\xi_{2j}}{d\overline{r}}\right) + M_{6j} + M_{7j}\xi_{2j} + M_{8j} + M_{9j}\xi_{1j} + M_{10j}\right]d\overline{r} = 0, p = 1,2 \tag{69}$$

$$\int_0^R x_p(\overline{r})\left[\begin{array}{l} N_{1j}\frac{1}{\overline{r}}\frac{d}{d\overline{r}}\left(\overline{r}\frac{d\xi_{2j}}{d\overline{r}}\right) + N_{2j} + N_{3j}\xi_{2j} + N_{4j} + N_{5j}\frac{d\xi_{2j}}{d\overline{r}}\frac{d\xi_{2j}}{d\overline{r}} + N_{6j}\frac{d\xi_{2j}}{d\overline{r}} + N_{7j}\frac{d\xi_{1j}}{d\overline{r}} + N_{8j} + N_{9j}\xi_{1j}\xi_{2j} + N_{10j}\xi_{2j} \\ +N_{11j}\xi_{1j} + N_{12j} + N_{13j}\left(\frac{d\xi_{2j}}{d\overline{r}}\right)^2 + N_{14j} + N_{15j}\frac{d\xi_{2j}}{d\overline{r}} + N_{16j}\xi_{2j}{}^2 + N_{17j} + N_{18j}\xi_{2j} + N_{19j}\xi_{2j} + N_{20j} \end{array}\right]d\overline{r} = 0, p = 1,2 \tag{70}$$
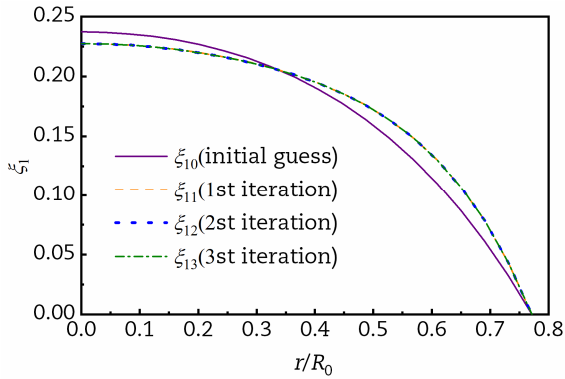
Table 1. Geometrical parameters in the numerical examples

$d_0 / R_0 = 1.4$	$m = 2$	$\delta / R_0 = 0.2$	$l_0 / R_0 = 1.4$	$L / R_0 = 3.6$

Table 2. Convergence of $\psi_1(\overline{z})$ and $\psi_2(\overline{z})$ for converging artery

	1st iteration	2nd iteration	3rd iteration
ψ_1	4.519	4.536	4.536
ψ_2	-1.352	-1.357	-1.357

Fig. 2. Convergence of $\xi_1(\overline{r})$ for converging artery
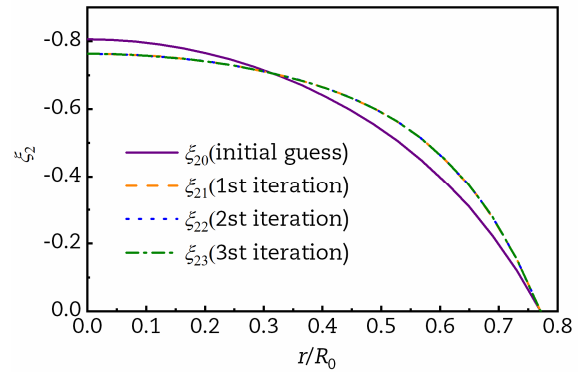
Fig. 3. Convergence of $\xi_2(\overline{r})$ for converging artery

After calculating the coefficients β_{ij} and placing them in Equations (66) and (67), values of functions ξ_{11}, ξ_{21} are obtained by placing these new values in Eqs. (53) and (54) and repeat the process of solving new values of functions $\psi_{1j}(\overline{z})$, $\psi_{2j}(\overline{z})$. The process iterates until convergence. The nth iteration gives the final values for temperature and concentration using Eqs. (48) and (49). Solving the above equations is done by Maple software. The constants F_{ij}, $M_{ij}, i = 1,..,10$ and $G_{ij}, N_{ij}, i = 1,..,20$ are presented in the Appendix.

Figures 2 and 3 and Table 2 respectively show the convergence of functions $\psi_1(\overline{z})$, $\psi_2(\overline{z})$, $\xi_1(\overline{r})$, and $\xi_2(\overline{r})$ based on the material and geometric properties in Table 1. These values are for a section of converging tapered artery ($\xi = -0.017$) with maximum stenosis. The dimensionless pressure gradient ($d\overline{P}/d\overline{z} = -29.17$) is selected according to [31] for the tapered artery with a taper angle of 1°. As observed, the Kantorovich method quickly converges, and after the third iteration, the function values cease to change.

3.3 Calculation of characteristic material length

The characteristic length parameter in couple stress theory depends on the fluid's geometry, boundary conditions, and material properties. The characteristic length can be calculated via experimental methods or dynamic molecular simulation. Stokes [14] was the first to introduce the couple stress theory of fluids. In his study, he proposed a method to estimate the characteristic length. In this method, using the experimental volumetric flow rate and equating it with the theoretical equation, the characteristic length is obtained:

$$Q_{exp} = AU = 2\pi \int_0^R r u \, dr \tag{71}$$

In case of missing experimental values, the characteristic length can be estimated via:

$$R^{*2} = \left(\frac{R}{R_0}\right)^2 = 2 \int_0^{R^*} \overline{r} \overline{u} \, d\overline{r} \tag{72}$$

The characteristic length can be determined by trial and error, using the velocity profile equation, and substituting it in Eq. (72).

4. Results and Discussion

4.1 Validation with experimental results

Figures 4 and 5 compare velocity profiles obtained by this theory and experimental results in [32] for two different flow rates. The velocity profiles represent stable blood flow with a hematocrit of 10% in a non-tapered artery without stenosis ($R_0 = 20$ μm). According to the experimental results, the power-law and consistency index of the blood fluid with a hematocrit of 10% are assumed n = 0.8796 and k = 0.002702 Pa/sn [33]. In Fig. 4, blood flow and pressure gradient mean velocity are $U = 3.9$ mm/s and dP / dz = 118.605 kPa/m, respectively. The theoretical result for the characteristic length is $L^* = 0.187$. This characteristic length is calculated using Eq. (72). In Fig. 4, the velocity profile of the classical theory ($L^* = 0$) and couple stress theory is compared with experimental results, indicating a better match between couple stress and experimental results compared to classical theory. The difference in velocity at the center of the artery between the experimental and the classical theory is 36%, while this value has been reduced to 14% for the couple stress theory results. Fig. 5 compares the results of couple stress theory (Eq. (41)) and classical theory and experimental results in [32] (mean speed: $U = 14.7$ mm/s, dP/dz = 473.077 kPa/m, $L^* = 0.31$). This characteristic

length is obtained via Eq. (72). Fig. 5 shows a better consistency between the couple stress theory and experimental results than classical theory. In Fig. 4 and 5, the difference between the couple stress theory and classical theories is significant. This difference entirely depends on the geometrics of the problem; that is, for smaller dimensions (micro and nano scales), the difference is significant while it is negligible for larger dimensions [34]. This shows the importance of using couple stress theory and characteristic length when dealing with the flow in small-scale geometries.

4.2 Velocity, concentration, and temperature profiles

Figures 6 and 7 show the dimensionless velocity profiles in non-tapered, converging, and diverging arteries with blood as a non-Newtonian fluid. The geometric parameters are as stated in Table 1. The taper gradient for diverging arteries, non-tapered, and converging arteries are $\xi / R_0 = 0.017$, $\xi / R_0 = 0$, and $\xi / R_0 = -0.017$, respectively. The pressure gradient is assumed $d\bar{P}/d\bar{z} = -29.17$ [31], and the velocity profile is for the arterial section with the highest stenosis.

Figure 6 shows variations in dimensionless velocity profile for three values of the power-law index ($n = 0.775$, $n = 0.8$, and $n = 0.85$) in converging, diverging, and non-tapered arteries. In all three geometries, the increase in the power-law index makes the flat velocity profile. Increasing the viscosity by increasing the power-law index near the wall leads to an increase in the velocity gradient in this area. As a result, the maximum velocity decreases at a constant flow rate within an artery with a specified geometry in these conditions. Further, as shown in Fig. 6, the diverging artery's velocity profile is higher than non-tapered and converging arteries for specific dimensionless pressure gradients. Therefore, increasing the radius of the artery increases both the pressure gradient and mean flow velocity at each section while maintaining a constant dimensionless pressure gradient (Eq. (19)). Table 3 shows the characteristic material length obtained from Eq. (72) for all three arterial geometries, including various power-law indices.

Figure 7 shows the influence of Darcy number on the dimensionless velocity profile in converging, diverging, and non-tapered arteries ($n = 0.8$). Increasing the Darcy number increases slip velocity on the arterial wall and velocity profile in all three geometries. Increasing the Darcy number leads to a reduced arterial radius, and in turn, increased velocity. The Darcy values $Da = 10^{-7}$ and $Da = 10^{-10}$ are selected from [35-37] according to the wall permeability and arterial radius.
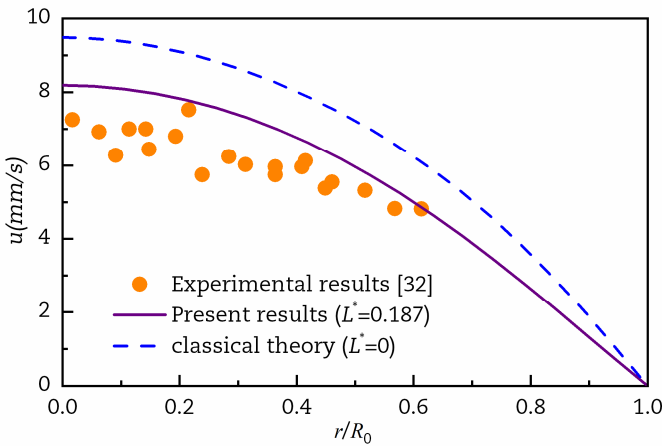

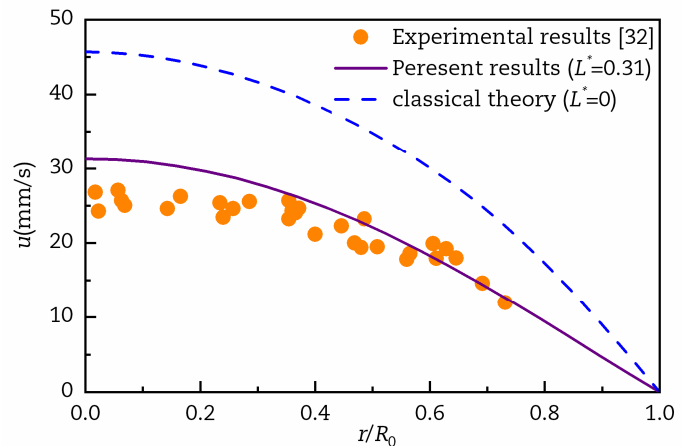**Fig. 4.** Comparison of theoretical velocity profile with experimental results [32] for mean velocity $U = 3.9 \, \text{mm/s}$

Fig. 5. Comparison of theoretical velocity profile with experimental results [32] for mean velocity $U = 14.7 \, \text{mm/s}$
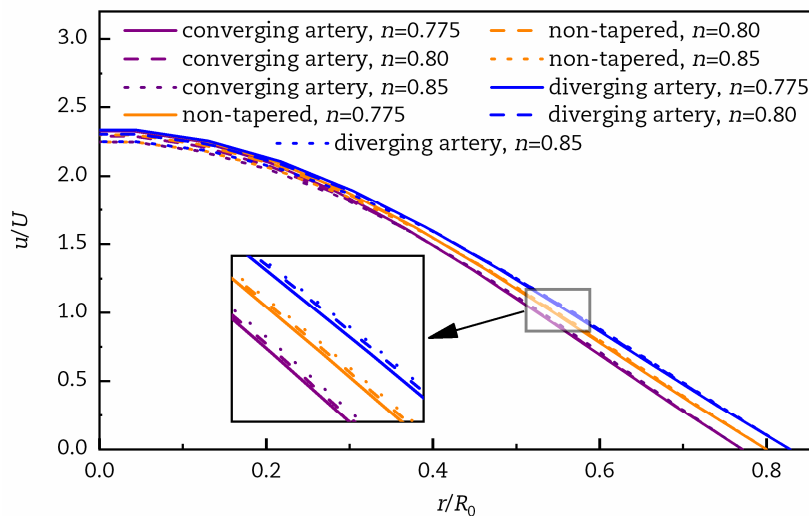

Fig. 6. Variation in velocity profile for $n = 0.775$, 0.8, and 0.85
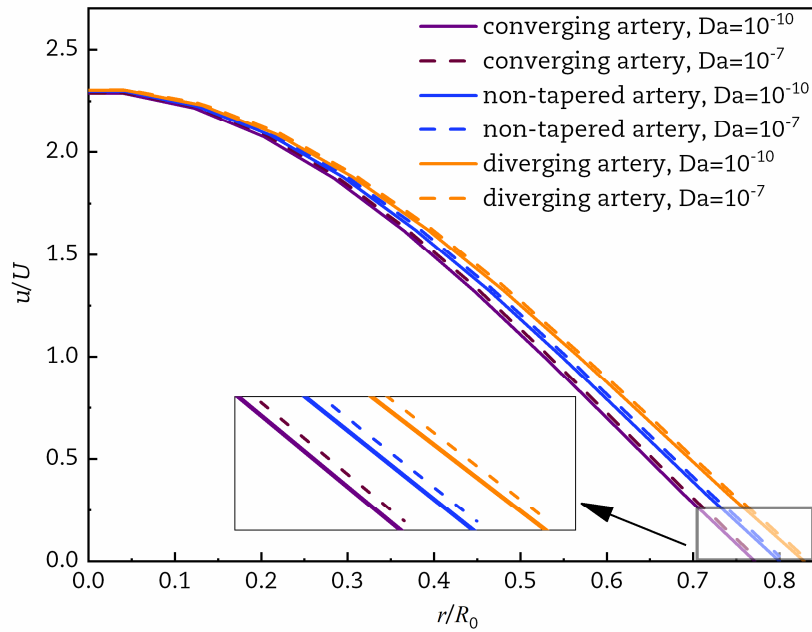
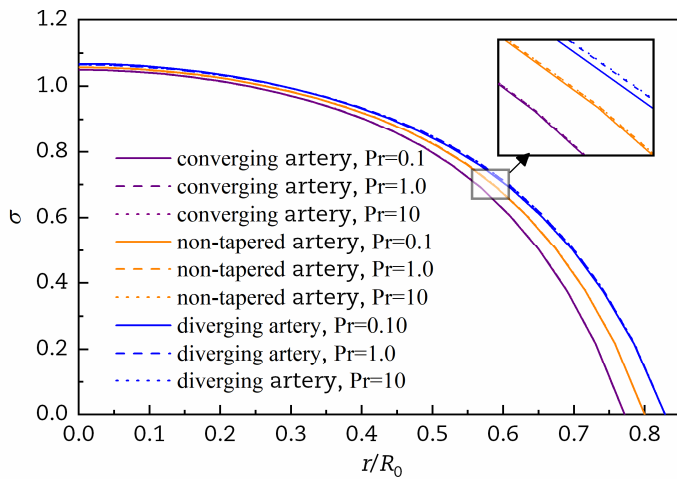**Fig. 7.** Influence of Darcy number (*Da*) on the velocity profile

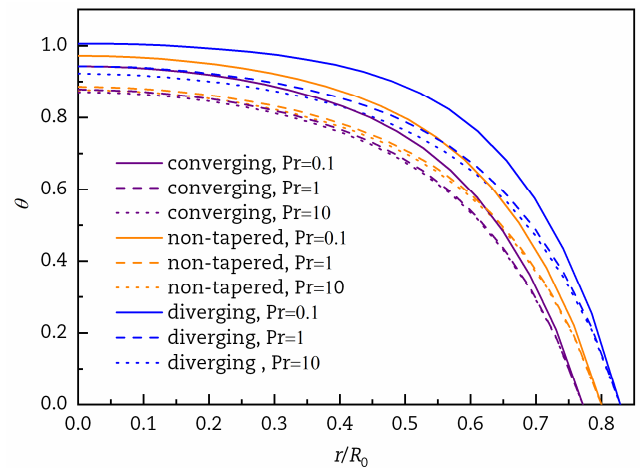**Fig. 8.** Influence of Prandtl number (Pr) on the concentration profile

Fig. 9. Influence of Prandtl number (Pr) on the temperature profile

Figures 8 and 9 show the variations in concentration and temperature profiles for different values of $Pr = 0.1$, 1 and 10 in diverging ($\xi / R_0 = 0.017$), non-tapered ($\xi / R_0 = 0$) and converging ($\xi / R_0 = -0.017$) arteries. This paper assumes the following parameter values: $N_b = N_t = 1$, $d\bar{P}/d\bar{z} = -29.17$, $Sc = 10$, $n = 0.8$, and $Re = 100$. Table 1 shows the respective geometric parameters. The power-law ($n = 0.8$) is based on 40% hematocrit in the blood of a healthy individual. Figure 8 shows how the concentration profile increases with an increase in the Prandtl number in all three arterial geometries. However, in Fig. 9, Increase in Prandtl number reduces the temperature. Reduced thermal permeability or fluid conductivity coefficient, in turn, reduces heat transfer and temperature. Although in Fig. 8, increasing the Prandtl number causes minor concentration variations, in Fig. 9, increasing the Prandtl number significantly increases the temperature.

Figures 10 and 11 respectively show the variations in dimensionless concentration and temperature profiles for $Sc = 1$ and 10 in the three geometries of diverging ($\xi / R_0 = 0.017$), non-tapered $\xi / R_0 = 0$), and converging ($\xi / R_0 = -0.017$) arteries and with $N_b = N_t = Pr = 1$, $d\bar{P}/d\bar{z} = -29.17$, $n = 0.8$, and $Re = 100$. Although Fig. 11 shows minor variations in temperature profile with increased Schmidt number, in Fig. 10, the gradient of the concentration curve (concentration gradient) close to the artery wall significantly increases with increased Schmidt number. In fact, reduced Brownian diffusion coefficient and constant Reynolds and Prandtl numbers—leading to a constant viscosity and flow velocity—increase viscosity effects close to the wall and, in turn, increase nanoparticle concentration. However, reduced viscosity effects also reduce concentration at the center of the artery.

Table 3. The calculated length scale for different values of *n*

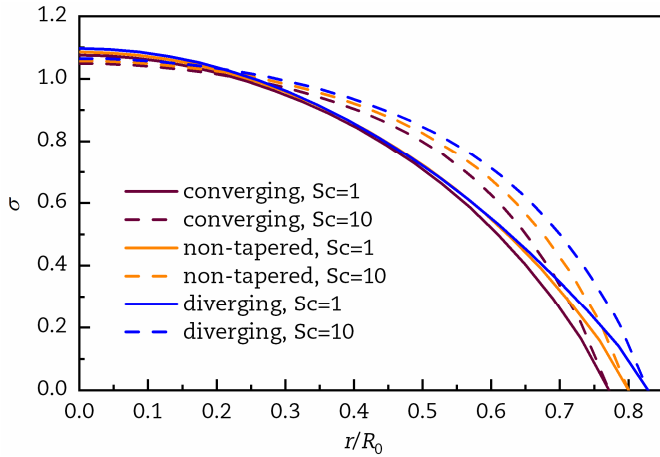|	$n = 0.775$	$n = 0.8$	$n = 0.85$
Converging artery	$\overset{.}{L} = 0.639$	$\overset{.}{L} = 0.55$	$\overset{.}{L} = 0.456$
Non-tapered artery	$\overset{.}{L} = 0.697$	$\overset{.}{L} = 0.6$	$\overset{.}{L} = 0.5$
Diverging artery	$\overset{.}{L} = 0.758$	$\overset{.}{L} = 0.652$	$\overset{.}{L} = 0.545$

Fig. 10. Influence of Schmidt number (Sc) on the concentration profile
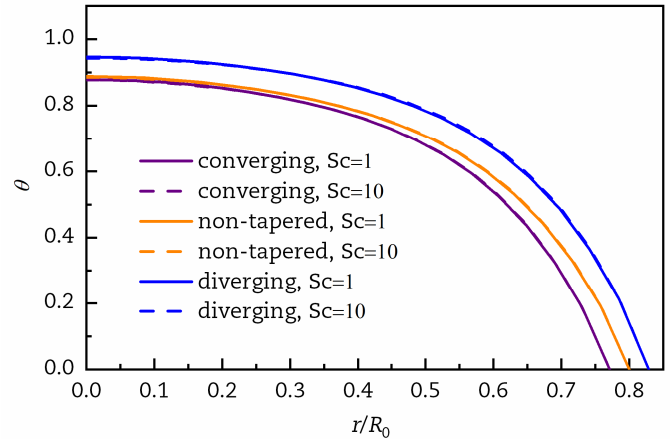

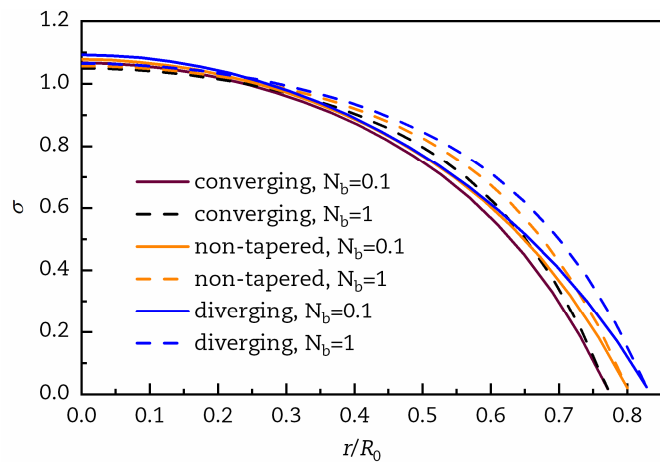**Fig. 11.** Influence of Schmidt number (Sc) on the temperature profile

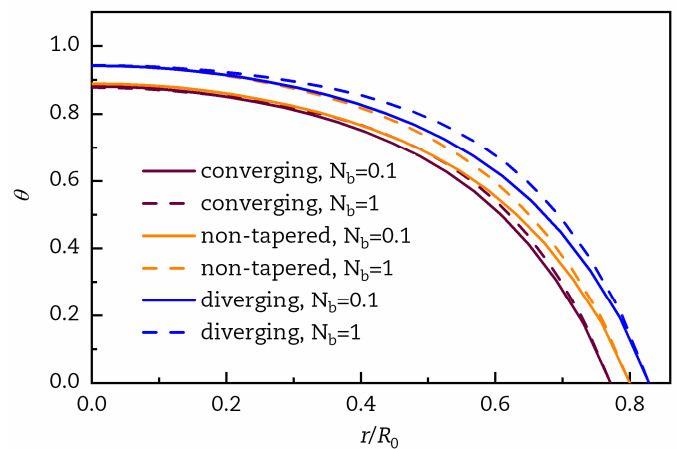**Fig. 12.** Influence of Brownian parameter (N_b) on the concentration profile

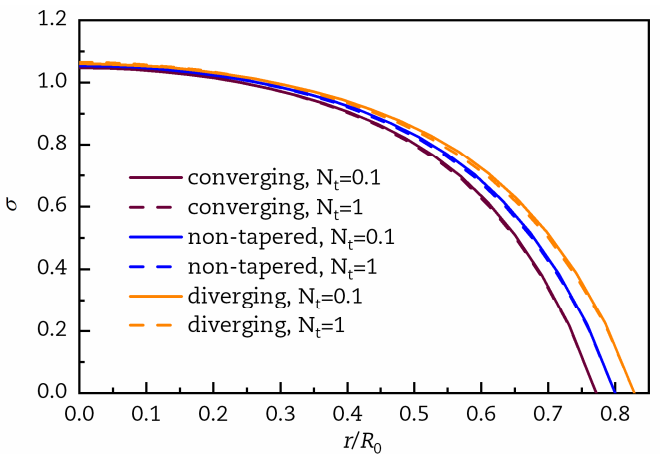**Fig. 13.** Influence of Brownian parameter (N_b) on the temperature profile

Fig. 14. Influence of thermophoresis parameter (N_t) on the concentration profile
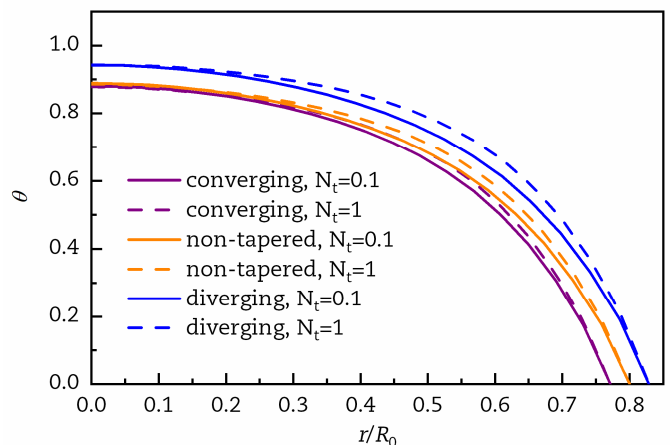

Fig. 15. Influence of thermophoresis parameter (N_t) on the temperature profile

Figures 12 and 13 show the variations in dimensionless concentration and temperature profiles with increasing N_b while assuming $N_t = \text{Pr} = 1$, $d\bar{P}/d\bar{z} = -29.17$, $n = 0.8$, $\text{Re} = 100$, and $Sc = 10$. Figure 12 shows the increased dimensionless concentration profile close to the wall with increased N_b; however, at the center of the artery, concentration is reduced. According to Eq. (19) and considering the constant values for Prandtl and Schmidt's numbers leading to a constant ratio between Brownian diffusion and thermal diffusion coefficients, the concentration gradient near the wall increases with increasing N_b. Figure 13 shows an increased dimensionless temperature profile with increased N_b. The Brownian movement of nanoparticles increases thermal conductivity, and in turn, the temperature.

Figures 14 and 15 respectively show the variations in dimensionless concentration and temperature profiles for N_t values of 0.1 and 1, $N_b = \text{Pr} = 1$, $d\overline{P}/d\overline{z} = -29.17$, $n = 0.8$, $\text{Re} = 100$, and $\text{Sc} = 10$. Figure 14 shows a reduced concentration profile with increased N_t; conversely, Fig. 15 indicates the opposite for the dimensionless temperature profile where increasing N_t also increases the temperature.

In Figs. 8-15, concentration and temperature profiles represent the arterial section with the highest stenosis. The dimensionless characteristic length for velocity profiles of each section has been obtained using Eq. (72) and Table 3 for a power-law index of $n = 0.8$.

5. Conclusion

Galerkin and extended Kantorovich methods were used to solve momentum equations and mass transfer and energy equations for power-law nanofluid flow in tapered and non-tapered arteries. Figs. 4 and 5 indicate a proper consistency between the velocity profiles obtained from the couple stress theory and previously obtained experimental findings compared to classical theories' results. According to Figs. 2 and 3 and Table 2, the convergence in the Kantorovich method for mass transfer and energy equations indicates its quick convergence in the third step.

The influence of parameters such as dimensionless Darcy number and Power-law on the velocity profile, as well as the effect of parameters such as dimensionless Prandtl and Schmidt numbers, the thermospheric parameter, and Brownian movement on dimensionless concentration and temperature profiles, were investigated. Overall, the effects of the above parameters on velocity, concentration, and temperature profiles can be described as follows:

1. The dimensionless velocity profile in all three arterial geometries increases with an increase in the Darcy number;
2. Increasing the power-law index flattens the velocity profile curve. As a result, the shear stress near the wall increases. Studies have shown that in areas of the artery where the shear stress is low, the accumulation of particle concentrations is higher and vice versa. Therefore, particles' accumulation near the wall decreases with the increasing Power-low index.
3. Increasing the Prandtl number also increases concentration profile while decreasing the temperature profile;
4. Increasing the Schmidt number also increases nanoparticle concentration close to arterial walls while reducing it at the center of arterial geometry; nevertheless, there is only a minor increase in temperature profile with increased Schmidt number;
5. Increasing the dimensionless Brownian parameter also increases the concentration profile near the arterial wall while reducing it near the center of arterial geometry. In addition, increasing the dimensionless Brownian parameter also increases the dimensionless temperature profile;
6. Increasing the dimensionless thermospheric parameter reduces the concentration profile while increasing the temperature profile.

The results of this study, especially the study of various parameters on the concentration of particles, can be effective in investigating the decreasing or increasing trend of particles within the artery. These particles can be fat particles such as LDLs or drug nanoparticles. Reducing the accumulation of fat particles in the wall is very important in reducing the stenosis of the arteries.

Author Contributions

All authors contributed equally, discussed the results, reviewed, and approved the final version of the manuscript.

Acknowledgments

Conflict of Interest

The authors declared no potential conflicts of interest concerning the research, authorship, and publication of this article.

Funding

Data Availability Statements

The datasets generated and/or analyzed during the current study are available from the corresponding author on reasonable request.

Nomenclature

A	Force stress tensor	V	Velocity vector
c	Volumetric volume expansion coefficient	l	Characteristic material length
C	Concentration	l_0	Length of stenosis
D_a	Darcy number	l_1	Length of artery
D_B	Brownian diffusion coefficient	M_{ij}	Coupe stress tensor
D_T	Thermospheric diffusion coefficient	m	Shape parameter
K_{nf}	Thermal conductivity	n	Power-law index
P	Pressure	N_b	Brownian motion parameter

Pr	Prandtl number	N_t	Thermophoresis parameter
R_0	The radius of the non-tapered artery	α	Slip parameter
$R(z)$	The radius of the tapered artery	α_1	Thermal diffusivity
Re	Reynolds number	δ	The height of the stenosis
Sc	Schmidt number	λ	Wall permeability coefficient
T	Temperature	μ	Viscosity
u	Axial velocity	ξ	Tapering parameter
v	Radial velocity	ρ	Density

References

[1] Ross, R., Atherosclerosis — an Inflammatory Disease, *New England Journal of Medicine,* 340(2), 1999, 115-126.

[2] Haldar, K., Effects of the shape of stenosis on the resistance to blood flow through an artery, *Bulletin of Mathematical Biology,* 47(4), 1985, 545-550.

[3] Nadeem, S. Akbar, N.S., Hendi, A.A., Hayat, T., Power law fluid model for blood flow through a tapered artery with a stenosis, *Applied Mathematics and Computation,* 217(17), 2011, 7108-7116.

[4] Liu, G.T., Wang, X.J. Ai, B.Q., Liu, L.G., Numerical Study of Pulsating Flow Through a Tapered Artery with Stenosis, *Chinese Journal of Physics,* 42(4), 2004, 401-409.

[5] Shukla, J.B., Parihar, R.S., Rao, B.R.P., Effects of stenosis on non-Newtonian flow of the blood in an artery, *Bulletin of Mathematical Biology,* 42(3), 1980, 283-294.

[6] Johnston, B.M., Johnston, P.R., Corney, S., Kilpatrick, D., Non-Newtonian blood flow in human right coronary arteries: steady state simulations, *Journal of Biomechanics,* 37(5), 2004, 709-720.

[7] Liu, B., Tang, D., Influence of non-Newtonian properties of blood on the wall shear stress in human atherosclerotic right coronary arteries, *Molecular & Cellular Biomechanics: MCB,* 8(1), 2011, 73-90.

[8] Chen, J., Lu, X.Y., Numerical investigation of the non-Newtonian blood flow in a bifurcation model with a non-planar branch, *Journal of Biomechanics,* 37(12), 2004, 1899-911.

[9] Mekheimer, K.S., Effect of the induced magnetic field on peristaltic flow of a couple stress fluid, *Physics Letters A,* 372(23), 2008, 4271-4278.

[10] Srinivasacharya, D., Srikanth, D., Effect of couple stresses on the flow in a constricted annulus, *Archive of Applied Mechanics,* 78(4), 2008, 251-257.

[11] Valanis, K.C., Sun, C.T., Poiseuille flow of a fluid with couple stress with applications to blood flow, *Bio Rheology,* 6(2), 1969, 85-97.

[12] Srivastava, L.M., Flow of couple stress fluid through stenotic blood vessels, *Journal of Biomechanics,* 18(7), 1985, 479-485.

[13] Srinivasacharya, D., Rao, G.M. Pulsatile flow of couple stress fluid through a bifurcated artery, *Ain Shams Engineering Journal,* 9(4), 2018, 883-893.

[14] Stokes, V.K., Couple Stresses in Fluids, *Physics of Fluids,* 9(9), 1966, 1709-1715.

[15] Pordanjani, A.H., Aghakhani, S., Afrand, M., Sharifpur, M., Meyer, J.P., Xu, H., Nanofluids: Physical phenomena, applications in thermal systems and the environment effects- a critical review, *Journal of Cleaner Production,* 320, 2021, 128573.

[16] Abidi, A., Ahmadi, A., Enayati, M., Sajadi, S.M., Yarmand, H., Ahmed, A., Cheraghian, G.A., Review of the Methods of Modeling Multi-Phase Flows within Different Microchannels Shapes and Their Applications, *Micromachines,* 12(9), 2021, 1113.

[17] Rostami, S., Aghakhani, S., Hajatzadeh Pordanjani, A., Afrand, M., Cheraghian, G., Oztop, H.F., Shadloo, M.S., A Review on the Control Parameters of Natural Convection in Different Shaped Cavities with and without Nanofluid, *Processes,* 8(9), 2020, 1011.

[18] Sheikhpour, M., Arabi, M., Kasaeian, A., Rokn Rabei, A., Taherian, Z., Role of Nanofluids in Drug Delivery and Biomedical Technology: Methods and Applications, *Nanotechnology, Science and Applications,* 13, 2020, 47-59.

[19] Cao, Q.L., Massoudi, M., Liao, W.H., Feng, F., Wu, W.T., Flow Characteristics of Water-HPC Gel in Converging Tubes and Tapered Injectors, *Energies,* 12(9), 2019, 1643.

[20] Karami, F., Ahmadi Nadooshan, A., Tadi Beni, Y., Development of the Couple Stress Relationships for the Power Law Fluid and the Solution of Flow in CeramicTape Casting Process, *Journal of Applied Fluid Mechanics,* 11(5), 2018, 1239-1246.

[21] Ellahi, R., Rahman, S.U., Nadeem, S., Blood flow of Jeffrey fluid in a catherized tapered artery with the suspension of nanoparticles, *Physics Letters A,* 378(40), 2014, 2973-2980.

[22] Rahman, S.U., Ellahi, R., Nadeem, S., Zia, Q.M.Z., Simultaneous effects of nanoparticles and slip on Jeffrey fluid through tapered artery with mild stenosis, *Journal of Molecular Liquids,* 218, 2016, 484-493.

[23] Akbar, N.S., Rahman, S.U., Ellahi, R., Nadeem, S., Nano fluid flow in tapering stenosed arteries with permeable walls, *International Journal of Thermal Sciences,* 85, 2014, 54-61.

[24] Reddy, J.V.R., Srikanth, D., The Polar Fluid Model for Blood Flow through a Tapered Artery with Overlapping Stenosis: Effects of Catheter and Velocity Slip, *Applied Bionics and Biomechanics,* 2015, 12.

[25] Akbar, N.S., Non-Newtonian model study for blood flow through a tapered artery with a stenosis, *Alexandria Engineering Journal,* 55(1), 2016, 321-329.

[26] Chakravarty, S., Mandal, P.K., Two-dimensional blood flow through tapered arteries under stenotic conditions, *International Journal of Non-Linear Mechanics,* 35(5), 2000, 779-793.

[27] Srivastava, V.P., Saxena, M., Suspension model for blood flow through stenotic arteries with a cell-free plasma layer, *Mathematical Biosciences,* 139(2), 1997, 79-102.

[28] Beavers, G.S., Joseph, D.D., Boundary conditions at a naturally permeable wall, *Journal of Fluid Mechanics,* 30(1), 2006, 197-207.

[29] Qiuyang, D., *Numerical Solutions of the Radiosity Equation by the Galerkin Method for the Spherical Pyramid (Mars Project),* Bachelor Thesis, Mathematics Department, Roger Williams University, Rhode Island, 2017.

[30] Suri, P.K., Suri, P.R., Effect of static magnetic field on blood flow in a branch, *Indian Journal of Pure and Applied Mathematics,* 12(7), 1931, 907-918.

[31] Belardinelli, E., Cavalcanti, S., A new nonlinear two-dimensional model of blood motion in tapered and elastic vessels, *Computers in Biology and Medicine,* 21(1), 1991, 1-13.

[32] Bugliarello, G., Sevilla, J., Velocity distribution and other characteristics of steady and pulsatile blood flow in fine glass tubes, *Biorheology,* 7(2), 1970, 85-107.

[33] Roe, E., Wells, Jr., E.W., Merrill, Influence of flow properties of blood upon viscosity-hematocrit relationships, *The Journal of Clinical Investigation,* 41(8), 1962, 1591-1598.

[34] Hadjesfandiari, A.R., Hajesfandiari, A., Dargush, G.F., Skew-symmetric couple-stress fluid mechanics, *Acta Mechanica,* 226(3), 2015, 871-895.

[35] Ai, L., Vafai, K., A coupling model for macromolecule transport in a stenosed arterial wall, *International Journal of Heat and Mass Transfer,* 49(9), 2006, 1568-1591.

[36] Murphy, J.D., Rabinovitch, M., Goldstein, J.D., Reid, L.M., The structural basis of persistent pulmonary hypertension of the newborn infant, *The Journal of Pediatrics,* 98(6), 1981, 962-967.

[37] Geddes, J., Carr, R., Karst, N., Wu, F., The Onset of Oscillations in Microvascular Blood Flow, *SIAM Journal on Applied Dynamical Systems,* 6(4), 2007, 694-727.

ORCID iD

Fatemeh Karami   https://orcid.org/0000-0002-3992-5612

Afshin Ahmadi Nadooshan https://orcid.org/0000-0003-4345-9527
Yaghoub Tadi Beni https://orcid.org/0000-0002-1645-6403

Publisher's Note Shahid Chamran University of Ahvaz remains neutral with regard to jurisdictional claims in published maps and institutional affiliations.